

See discussions, stats, and author profiles for this publication at: <https://www.researchgate.net/publication/353834458>

Joint Inversion of Rupture across a Fault Steptover during the 8 August 2017 Mw 6.5 Jiuzhaigou, China, Earthquake

Article in *Seismological Research Letters* · August 2021

DOI: 10.1785/0220210084

CITATIONS

2

READS

164

6 authors, including:



Wanpeng Feng

Sun Yat-Sen University

76 PUBLICATIONS 1,045 CITATIONS

[SEE PROFILE](#)



Jieyuan Ning

Peking University

124 PUBLICATIONS 1,744 CITATIONS

[SEE PROFILE](#)

Some of the authors of this publication are also working on these related projects:



国家自然科学基金 (4 1 8 7 4 0 7 1 , 4 1 3 7 4 0 4 7) 资助 [View project](#)



tsunami detection [View project](#)

Joint Inversion of Rupture across a Fault Stepover during the 8 August 2017 M_w 6.5 Jiuzhaigou, China, Earthquake

Yong Zhang^{*1}, Wanpeng Feng^{2,3}, Xingxing Li⁴, Yajing Liu⁵ , Jieyuan Ning¹, and Qinghua Huang¹

Abstract

The 8 August 2017 M_w 6.5 Jiuzhaigou earthquake occurred in a tectonically fractured region in southwest China. We investigate the multifault coseismic rupture process by jointly analyzing teleseismic, strong-motion, high-rate Global Positioning System, and Interferometric Synthetic Aperture Radar (InSAR) datasets. We clearly identify two right-stepping fault segments and a compressional stepover based on variations in focal mechanisms constrained by coseismic InSAR deformation data. The average geometric parameters of the northwest and southeast segments are strike = 130° /dip = 57° and strike = 151° /dip = 70° , respectively. The rupture model estimated from a joint inversion of the seismic and geodetic datasets indicates that the rupture initiated on the southeastern segment and jumped to the northwestern segment, resulting in distinctive slip patches on the two segments. A 4-km-long coseismic slip gap was identified around the stepover, consistent with the aftershock locations and mechanisms. The right-stepping segmentation and coseismic rupture across the compressional stepover exhibited by the 2017 Jiuzhaigou earthquake are reminiscent of the multifault rupture pattern during the 1976 Songpan earthquake sequence farther south along the Huya fault system in three successive $M_s \sim 7$ events. Although the common features of fault geometry and stepover may control the similarity in event locations and focal mechanisms of the 2017 and 1976 sequences, the significantly wider (~ 15 km) stepover in the 1976 sequence likely prohibited coseismic rupture jumping and hence reduced seismic hazard.


Cite this article as Zhang, Y., W. Feng, X. Li, Y. Liu, J. Ning, and Q. Huang (2021). Joint Inversion of Rupture across a Fault Stepover during the 8 August 2017 M_w 6.5 Jiuzhaigou, China, Earthquake, *Seismol. Res. Lett.* **XX**, 1–12, doi: [10.1785/SRL202010084](https://doi.org/10.1785/SRL202010084).

[Supplemental Material](#)

Introduction

The Bayan Har block at the easternmost Tibet plateau is bounded by several large-scale active faults on the boundaries, including the Kulun Shan fault to the north, the Garze–Yushu and Xianshuihe faults to the south, and the Longmen Shan thrust fault to the east (Fig. 1). Since 1997, eight strong earthquakes (M_w 6.5) have occurred around the block boundaries as a result of the eastward motion of the Bayan Har block, for example, the 2008 M_w 7.9 Wenchuan earthquake (Fig. 1; Diao *et al.*, 2010). At the northeastern corner of the Bayan Har block, several active faults (including the Longmen Shan, Mingshan, Huya [HYF], and Tazang faults [TZF]) intersect each other, showing localized complex surface motions with variable strain accumulation rates across the faults (Fig. 2; Ren *et al.*, 2013; Xu *et al.*, 2017). In the region, the HYF and the TZF are two adjacent left-lateral strike-slip faults, in which the HYF has been more seismically active than the TZF in recent decades. Four strong earthquakes ($M_w > 6$) occurred on HYF in the 1970s (Jones *et al.*, 1984; Zhu and Wen, 2009; Fig. 2). In particular, three strong earthquakes among them successively occurred along the HYF in

Songpan County over the course of a week in August 1976. Two of the three shocks had oblique-slip mechanisms, and the third was a pure thrust event. The variable fault mechanisms and aftershock locations of the three earthquakes indicate that the rupture of the first event on the 16 August 1976 event failed to jump through a compressional stepover, which caused a short delay before the following two large events coming (Jones *et al.*, 1984). To the north of the 1970s Songpan earthquakes where it is located between TZF and HYF, however, no active faults had previously been mapped, and no strong earthquakes had been recorded before the 2017 mainshock, raising the critical question as to whether this particular

1. School of Earth and Space Science, Peking University, Beijing, China;
2. Guangdong Provincial Key Laboratory of Geodynamics and Geohazards, School of Earth Sciences and Engineering, Sun Yat-Sen University, Guangzhou, China;
3. Southern Marine Science and Engineering Guangdong Laboratory (Zhuhai), Zhuhai, China;
4. School of Geodesy and Geomatics, Wuhan University, Wuhan, China;
5. Department of Earth and Planetary Science, McGill University, Montréal, Canada,  <https://orcid.org/0000-0002-5323-8077> (YL)

*Corresponding author: zhang-yong@pku.edu.cn

© Seismological Society of America

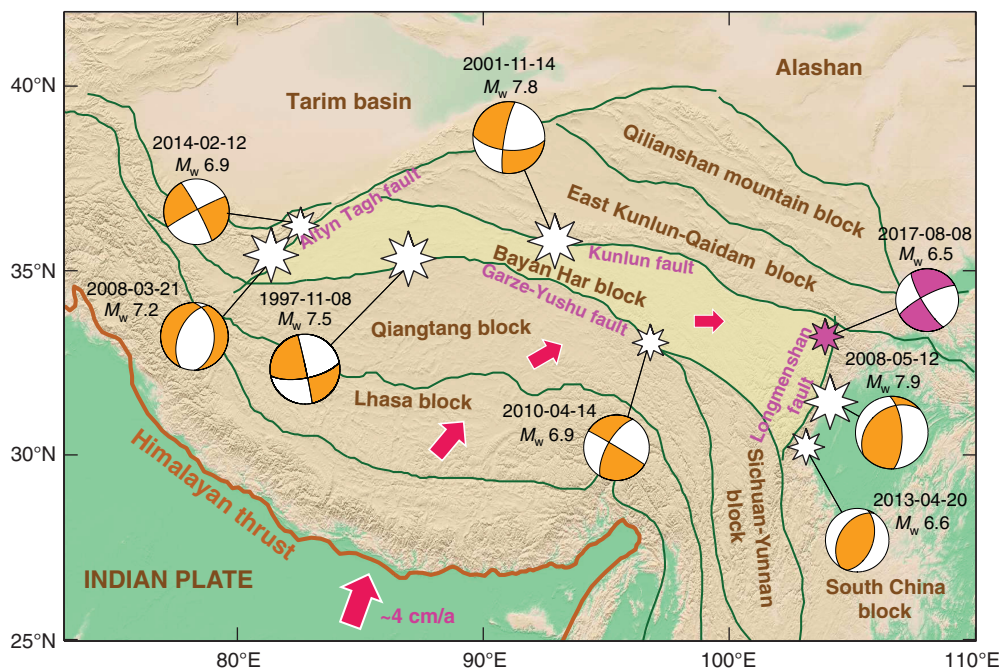


Figure 1. Tectonics of the Bayan Har block and surrounding regions. Stars and focal mechanism plots show the epicenters and mechanisms of the eight significant earthquakes that occurred at the boundaries of the block in 1997–2017.

section is also capable of hosting strong earthquakes and potentially linking the TZF and HYF segments.

The 8 August 2017 M_w 6.5 Jiuzhaigou earthquake is the largest earthquake in the northeast corner of the Bayan Har block in the past 40 yr. From China Earthquake Network Center (CENC), this earthquake initiated at 33.02° N, 103.82° E, at a depth of 20 km. It occurred precisely in the seismic “gap” between the TZF and HYFs, which effectively connects the aftershock zones of the 1970s Songpan earthquakes to the south (Fig. 2). The surface-wave magnitudes determined by CENC and the U.S. Geological Survey (USGS) are M_s 7.0 and M_s 6.8, respectively. In contrast, the moment magnitude derived from geodetic and seismic inversions ranges from M_w 6.4 to 6.5 (Yi *et al.*, 2017; Zhang, Feng, *et al.*, 2017; Zheng *et al.*, 2017; Han *et al.*, 2018; Xie *et al.*, 2018). The relatively large surface-wave magnitudes indicate a shallow centroid depth and energy focusing near surface. Through field investigations performed by the China Earthquake Administration (CEA), the maximum intensity in the epicentral area reached IX. Strong ground motions of the earthquake triggered serious surface damages in the region, leading to 25 deaths and >500 people injured.

Much attention has been drawn to the 2017 Jiuzhaigou earthquake on the seismogenic fault of the event, the rupture process, and its relation to the 1976 Songpan earthquake sequence. Among these issues, the fault geometry is a basic problem to be investigated. The aftershock relocation results indicate

a considerable complexity of the fault geometries. Multiple segments have been found from early aftershocks within 5 hr after the mainshock (Zhang, Feng, *et al.*, 2017). The dips of the different segments may be also different because the aftershocks are more scattered in the northwest than in the southeast (Fig. 2; Fang *et al.*, 2018). However, it is often challenging to solve this issue by separating the source parameters of each subevent because they occur within a very short time period in multiple rupture processes. Because no active faults were previously mapped in the epicentral area and no surface ruptures were reported after the earthquake, the earthquake faults that were fully based on the individual data in the previous published studies remain significantly different. Through

the inversion of Interferometric Synthetic Aperture Radar (InSAR) deformation data, Ji *et al.* (2017) assumed two fault segments that were vertical at shallow depth and dipped about 60° – 70° to the northeast at depth. By contrast, three segments with different mechanisms were required in analyzing the InSAR and teleseismic data by Sun *et al.* (2018). Because the fault geometric model is critical and fundamental for understanding the earthquake source process, it is necessary to better constrain the complexities of the fault geometry, which will be subsequently applied to the investigation of the rupture process.

In this study, we investigate the 2017 Jiuzhaigou mainshock by combing the teleseismic, local strong-motion, high-rate Global Positioning System (GPS), and InSAR observations (Fig. 2). Slip modeling of the earthquake is conducted in two steps. In the first step, we construct a fault geometry model by inverting InSAR data assuming 2D variations in mechanisms. Based on the fault geometry model obtained in the previous step, we then jointly invert the teleseismic, local strong-motion, high-rate GPS, and InSAR data for the coseismic slip process. Its tectonophysical implications along the HYF are addressed in the Discussion section.

Geodetic Inversion of the Fault Geometry

Method and data

Significant differences can be found in the existing fault models of the Jiuzhaigou earthquake that were used in finite-fault

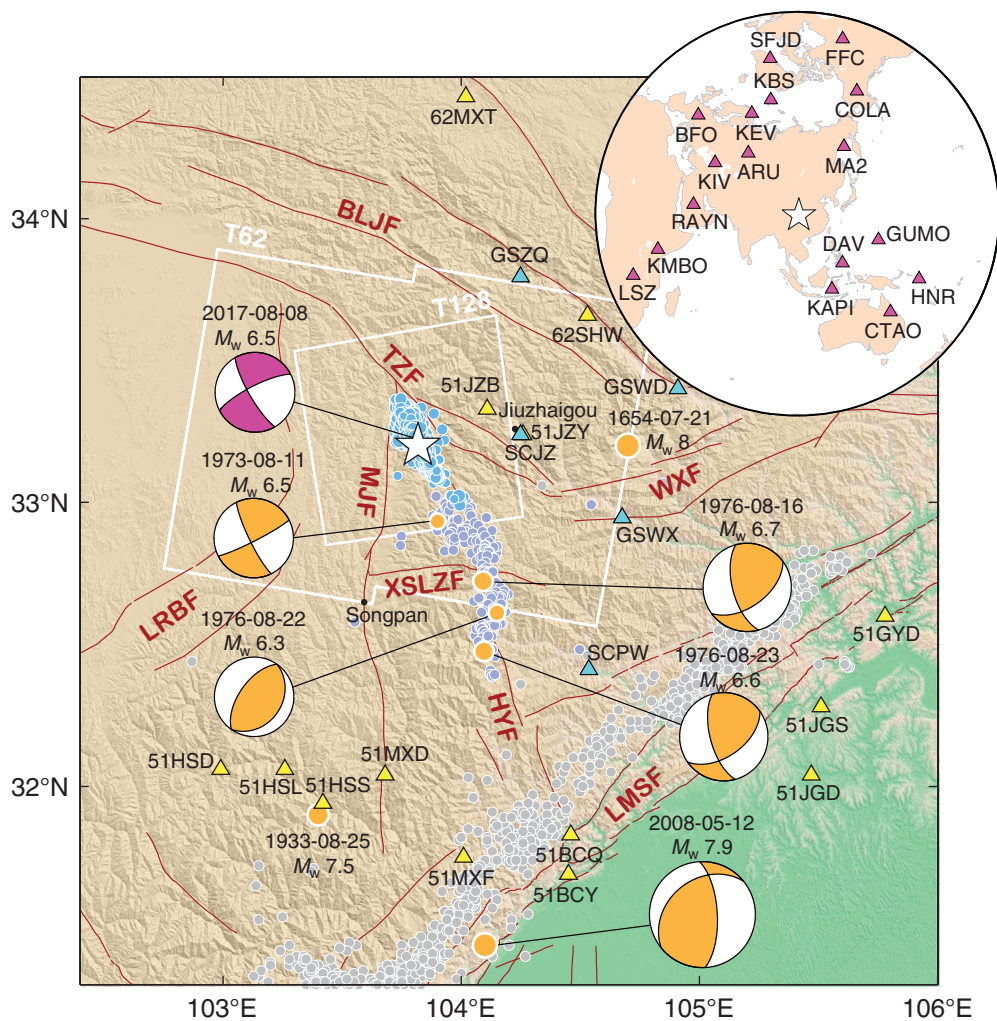


Figure 2. Map view of the northeastern corner of the Bayan Har block. Yellow circles are previous significant earthquakes in the area. The white star denotes the epicenter of the 2017 Jiuzhaigou earthquake. Cyan, blue, and gray circles are aftershocks of the 2017 Jiuzhaigou earthquake (Fang *et al.*, 2018), the 1976 Songpan earthquake sequence (Jones *et al.*, 1984), and the 2008 Wenchuan earthquake (Huang *et al.*, 2008), respectively. Yellow and cyan triangles denote the strong-motion (SM) stations and high-rate Global Positioning System (GPS) stations, respectively. Red lines are active faults (Deng *et al.*, 2003); the names of some major faults are labeled. The inset at the upper-right corner shows the teleseismic stations (triangles) and the epicenter of the 2017 Jiuzhaigou earthquake. BLJF, Bailongjiang fault; HYF, Huya fault; LMSF, Longmen Shan fault; LRBF, Longriba fault; MJF, Mingjiang fault; TZF, Tazang fault; WXF, Wenxian fault; XSLZF, Xueshanliangzi fault.

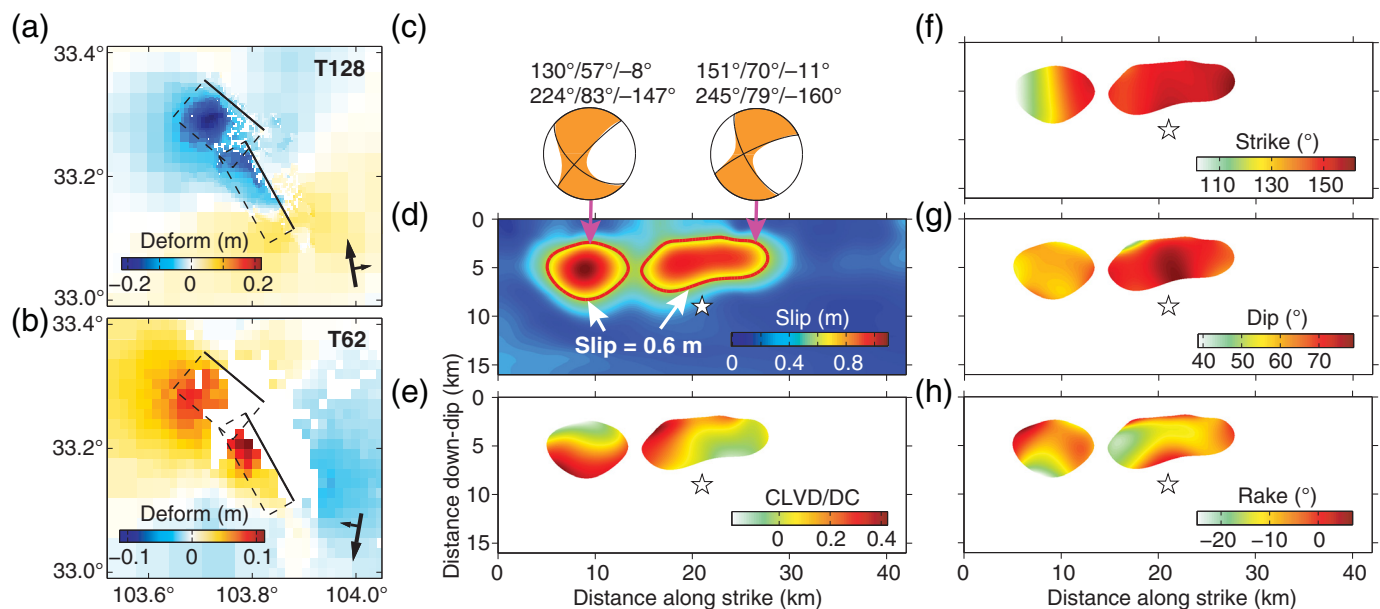
inversions (see Table 1). In early research, one segment was often considered (e.g., Zhang, Feng, *et al.*, 2017; Zheng *et al.*, 2017). However, both the relocated aftershocks and InSAR deformation suggest that the fault model may be complex and cannot be simplified as a single segment. In this work, we invert InSAR data to explore possible complexity in the fault model of the earthquake.

The complexity in fault geometry manifests in the heterogeneities of geometric parameters (i.e., strike and dip), which can be revealed by subevent seismic moment tensors. We use

the geodetic inversion method developed by Zhang and Wang (2015) to determine the subevent moment tensors. In this method, the positions of the subevents need to be fixed in advance. Because there is no prior knowledge of the fault geometric complexity, a planar fault is usually assumed and equally divided into subfaults, which are modeled as point sources. The subfault moment tensors can be solved by inverting geodetic deformation data, and thus the strikes, dips, rakes, and compensated linear vector dipoles (CLVDs) of each subfault can be obtained. These geometric parameters can reveal effective information of the complex fault geometric shape, although their locations are fixed on a planar fault. For cases of non-planar faults, some errors of the subfault locations would result. However, the influence of the location errors has been proved to be insignificant to the variable mechanisms (Zhang and Wang, 2015; Zhang, Wang, *et al.*, 2017).

The geodetic coseismic InSAR deformation data were used to investigate the complexity in fault geometry of the 2017 Jiuzhaigou event. We processed the Sentinel-1 Terrain Observation by Progressive Scan (TOPS) Synthetic Aperture Radar (SAR) data in tracks of T128

and T62 (Table S1, available in the supplemental material to this article) to map the coseismic deformation of the Jiuzhaigou earthquake. As a result of the emergency response of the European Space Agency, the T128 coseismic InSAR pair was available three days after the mainshock. The selected T62 InSAR pair (Table S1) shows fewer atmospheric effects than the other potential T62 coseismic pair having an even shorter temporal baseline. The 12 m resolution digital elevation model data produced with TanDEM-X SAR were used in data alignment and topographic phase removal. An automated InSAR



processing system (Feng *et al.*, 2017) was used in the data processing. Finally, 2376 and 3190 sample points were extracted from the two interferograms using a quadtree downsampling method (Simons *et al.*, 2002) for earthquake modeling.

Subfault moment tensor solutions and fault model

A 42 km × 16 km fault plane was assumed for the inversion. Following the practice of Zhang, Wang, *et al.* (2017), we first used a relatively large subfault size of 2 km × 2 km to search for the position, overall strike, and overall dip of the fault plane. As Figure S1 shows, a global minimum was reached at overall strike and dip angles of 154° and 68°, respectively (green rectangles in Fig. 3a,b). Then the optimized fault plane was further discretized into smaller 0.333 km × 0.333 km subfaults. The resulted subfault mechanism model, which explains the observed surface deformation (Fig. S2), suggests strong spatial heterogeneities not only in fault slips but also in the geometric parameters (Fig. 3). Two isolated slip patches are clearly distinguishable. One is located near the hypocenter, and the other

is 7–16 km to the northwest of the epicenter (Fig. 3d). Significant non-double-couple components (large CLVD) were found near the slip gap (Fig. 3e). The strike increases from ~110° in the northwest to >150° in the southeast (Fig. 3f),

TABLE 1

Fault Models and Data Used in Several Studies on the Joint Finite-Fault Inversions of the 2017 Jiuzhaigou Earthquake

Studies	Fault Model	Data
Sun <i>et al.</i> (2018)	Three segments (InSAR deformation and mechanism)	Teleseismic + InSAR
Zheng <i>et al.</i> (2020)	Two segments (aftershocks)	Teleseismic + InSAR+ strong motion
Zhang <i>et al.</i> (2021)	Single segment (mechanism)	Teleseismic + InSAR+ strong motion + local seismic
This study	Two segments (InSAR inversion)	Teleseismic + InSAR+ strong motion + hrGPS

The main bases are presented in the brackets below each fault model. hrGPS, high-rate Global Positioning System; InSAR, Interferometric Synthetic Aperture Radar.

suggesting complex fault segmentations. The dips are 55° – 60° in the northwest and 70° – 80° in the southeast (Fig. 3g). The gentle dips in the northwest coincide well with the scattered aftershocks that occurred there (Fang *et al.*, 2018). Unlike the strike and dip, no systematic change was observed in the rake angle (Fig. 3h). When only considering the subfault moment tensors with slips >0.6 m, the averaged fault parameters of the two slip patches are strike = 130° /dip = 57° /rake = -8° and strike = 151° /dip = 70° /rake = -11° , respectively. The differences in the strike and dip of the two patches are $\sim 21^{\circ}$ and 13° , respectively, suggesting that at least two fault segments were ruptured during the earthquake.

With the average geometric fault parameters of the two slip patches, we constructed a two-segment fault model by optimizing the segment positions along the southwest–north-east direction (black rectangles in Fig. 3a,b). It suggests a right-stepping segmentation of the earthquake fault. The two-segment fault model is consistent with the distribution of early aftershocks (within 5 hr; Fig. S3) and is similar to the model obtained by Zheng *et al.* (2020). It is possible that the two right-stepping and left-lateral strike-slip segments are linked by a thrust segment in the slip gap. However, the position of the thrust segment is unknown because no coseismic slip was found (Fig. 3d).

Joint Inversion of the Rupture Process Data and method

Based on the constructed two-segment fault model, we performed a joint inversion of rupture process by combining the teleseismic, local strong-motion, high-rate GPS, and InSAR data. The teleseismic data were downloaded from the Incorporated Research Institutions for Seismology data center. Telesismic stations with epicentral distances between 30° and 90° from the Global Seismographic Network were considered. To ensure an even azimuthal coverage surrounding the epicenter, the stations were reselected to ensure a minimum interval of 15° for takeoff and azimuth angles. Finally, the P waves on vertical components of 24 stations were obtained (Fig. 2).

A total of 66 strong-motion stations with three-component recordings were available from the China Strong Motion Network Center at the Institute of Engineering Mechanics, CEA. By considering the trade-off between station coverage and data quality, we chose 14 stations with epicentral distances ranging from 30 to about 200 km (Fig. 2).

We also processed continuous GPS data from five stations with epicentral distances between 40 and 110 km (Fig. 2). The epoch-wise positions for all the GPS stations were estimated using the kinematic precise point positioning (PPP) technique (Li, Ge, Zhang, *et al.*, 2013). Because the position before the earthquake was well known, the changes in positions can be easily obtained by subtracting the known position from the kinematic PPP solutions (Li, Ge, Guo, *et al.*, 2013). The GPS displacement time series and the strong-motion

data were grouped together in the joint inversion as “local waveform data.”

The constructed two-segment fault was used in the joint inversion. The two fault segments (sizes of which were assigned as $14\text{ km} \times 16\text{ km}$ and $18\text{ km} \times 16\text{ km}$; rectangles in Fig. 3a,b) were divided into $2\text{ km} \times 2\text{ km}$ subfaults. Because the differences between the CENC and USGS hypocentral locations are obvious in both horizontal and depth directions (Zheng *et al.*, 2017), the subfaults within 3 km of the CENC epicenter (33.20° N , 103.82° E) along the strike were allowed to rupture as early as possible (see the shadow area in Fig. 4d). That is, the rupture can initiate in an area instead of at a point. This practice helps to recover ruptures that might be biased by an incorrect hypocentral location (Zhang *et al.*, 2015).

The rupture model was determined using a linear inversion approach of Zhang *et al.* (2012). We jointly invert the waveform data (teleseismic, strong-motion, and high-rate GPS) and the geodetic deformation data (InSAR) for the rupture process. In the inversion of rupture process, the subfault source time functions (STFs) were modeled in a linear way. Meanwhile, a maximum rupture velocity of 3.5 km/s and a maximum rupture duration of 10 s were assumed to limit the time window of subfault STFs (Zhang *et al.*, 2012). This means that for a subfault d km away from the rupture initiation, the rupture velocity can range between 3.5 and $d/(d/3.5 + 10)$ km/s. Because the teleseismic and local waveform data have a good distribution on both the azimuthal and takeoff angles of the source and the deformation data well cover the entire coseismic deformation area (Figs. 2 and 3a,b), we equally weighted the waveform data and deformation data in the inversion. After the inversion, the teleseismic waves were shifted to best correlate their synthetics. We align the teleseismic data because they constrain only the relative position of fault slips compared with the hypocenter. In contrast, the strong-motion and high-rate GPS data were not aligned because they can constrain the absolute slip positions.

The seismic Green's functions were calculated based on the local crustal structure that was incorporated into CRUST2.0 (Table S2; Bassin *et al.*, 2001) and a global mantle model (Kennett *et al.*, 1995) using the codes developed by Wang *et al.* (2017)). Both the teleseismic velocity data and the strong-motion acceleration data were integrated into displacement waves. A band-pass filter of 0.02–0.4 Hz was applied to the teleseismic data. In contrast, the local waveform (strong-motion and high-rate GPS) data were filtered with 0.04–0.12 Hz. The lower cutoff frequency (0.04 Hz) was used because the baseline shifts in the strong-motion waves and the errors in the high-rate GPS data at low frequencies are more serious than those in the teleseismic data. The upper cutoff frequency (0.12 Hz) is to clear part of the surface waves. These surface waves, at a dominant period of about 7 s, are speculated to be caused by topographic effects and thus cannot be well fitted by synthetics based on a 1D-layered medium

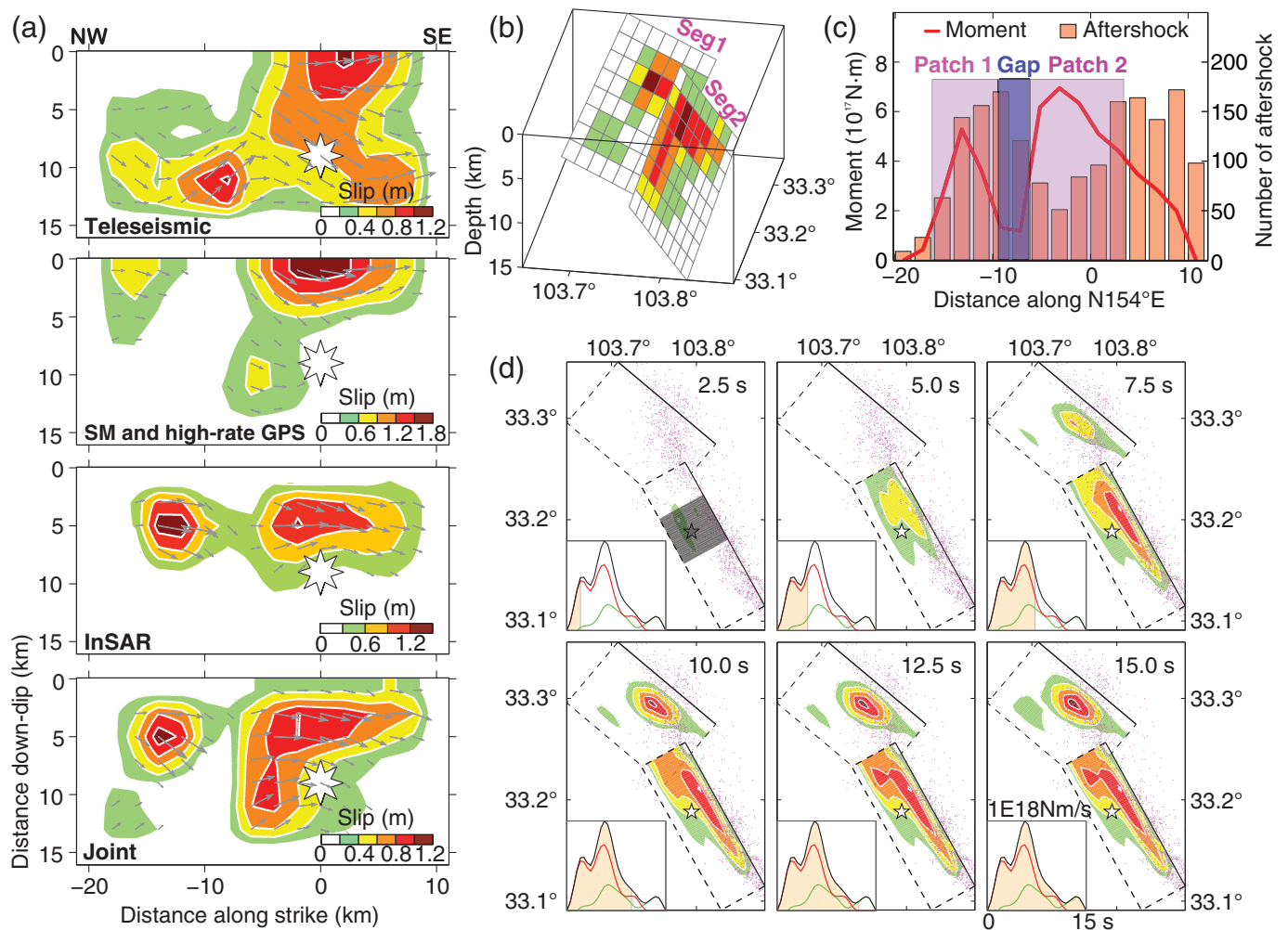


(Fig. S4). We also performed another joint inversion by suppressing the local surface waves with a taper and using a filter of 0.04–0.4 Hz (see Fig. S5). The results were similar to those of the full waveform inversion with a filter of 0.04–0.12 Hz (Fig. S5).

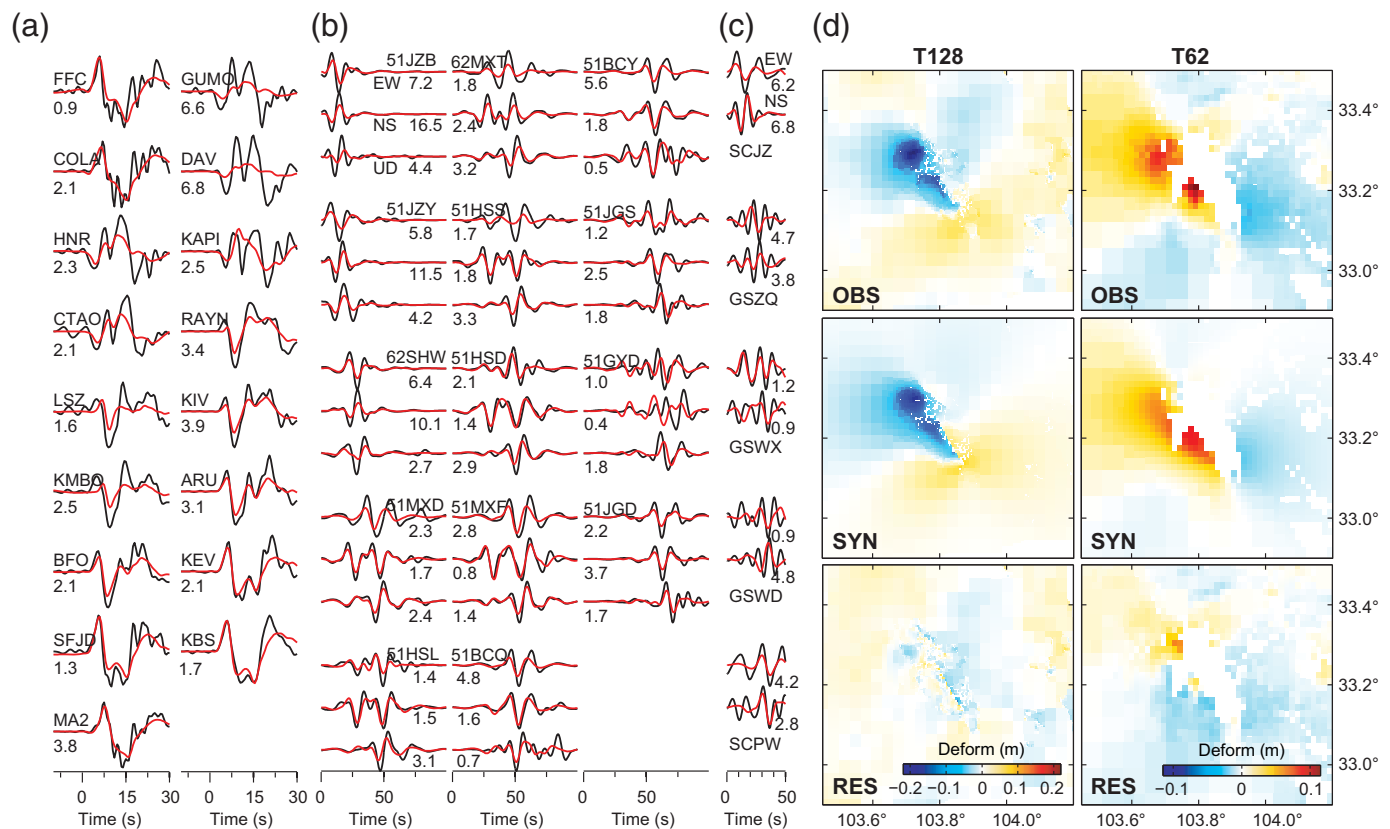
Rupture model

Two-patch slip pattern can be consistently found from inversions with individual datasets (Fig. 4a). In the teleseismic slip model, the northwest slip patch is ~10 km from the epicenter. The slip distribution appears to be relatively smooth most likely because of the low spatial resolution of the teleseismic data. The slip model produced by the local waveform (strong-motion and high-rate GPS) inversion suggests shallower slips, and the northwest slip patch is ~16 km away from the epicenter. In the InSAR model, most slips are located at depths of 3–7 km, and the northwest slip patch is ~12–14 km away from the epicenter. From the joint inversion, the shallower slip (depth 3–7 km) is close to the InSAR model, and the deeper slip (depth 7–13 km) is mainly consistent with the local waveform model. The depth-variable resolution of slip by different datasets is mainly caused by the decreasing resolution of local

Figure 4. (a) Slip models from the inversions of the different datasets. (b) 3D view of the slip model of the joint inversion. (c) Moment distribution and aftershock activity along the southeast direction. (d) Temporal variations of the surface projection of the slip distributions from the joint inversion. Gray rectangles represent the rupture initiation area. Insets at the bottom-left corners show the source time function. Green and red curves are the source time functions of the northwest and southeast segments, respectively.

surface deformation data with depth. The slip did not break through the ground surface, which may be caused by the limited seismogenic zone around the rupture area (Weng and Yang, 2017).

The mainshock seismic moment and aftershock activity show complementary patterns along the northwest–southeast direction (Fig. 4c). The aftershocks are more active around the northwest slip patch. This may be associated with the more heterogeneous fault geometry on the northwest segment. As shown in Figure 3f, the strike of the northwest segment changes from 110° to 150°, which can act as a geometric barrier (Das, 2007; Bouchon and Karabulut, 2008). This barrier may



have affected the mainshock rupture, causing heterogeneous residual stresses that favor the nucleation of abundant aftershocks. In contrast, the change in fault geometry of the southeast segment is not evident. This helps to fully release the stress during the mainshock, contributing to a higher seismic moment and hence fewer aftershocks (Bouchon and Karabulut, 2008). Aftershock activity is particularly high near the slip gap, possibly caused by the stress concentration as rupture approaches geometric heterogeneities (Saucier *et al.*, 1992; Das and Henry, 2003; Oglesby, 2005).

The temporal variations of the fault-slip distributions are depicted in Figure 4d. In the first 5 s after the earthquake initiation, the slips were mainly concentrated at 0–10 km on the southeast segment. From 5–10 s, the rupture expanded to a broad area on the southeast segment and simultaneously jumped to the northwest segment. After 10 s, the deep part of the southeast segment began to rupture and accumulated slip comparable to that at shallower depths. The average speed of the northwestward rupture propagation from the southeast segment to the northwest segment was ~ 2.7 km/s. Detailed rupture velocities are difficult to determine because of the uncertainty of the hypocenter. Thus, whether or not the barrier between the two segments has caused supershear (Weng *et al.*, 2015) on the northwest segment is indistinguishable. The released seismic moment was $\sim 5.2 \times 10^{18}$ N·m, which is equivalent to a magnitude of M_w 6.4. The northwest and southeast segments released about one-third and two-thirds of the total mainshock seismic moment, respectively.

Figure 5. Comparisons between the observed and synthesized data. (a) Teleseismic data, (b) strong-motion data, (c) high-rate GPS data, and (d) Interferometric Synthetic Aperture Radar (InSAR) data. The observed and synthesized waves in panels (a)–(c) are represented by black and red lines, respectively. Numbers in panels (a)–(c) denote the maximum amplitudes of the observed waves. The unit is micrometer in panel (a) and millimeter in panels (b,c).

Comparisons between the observations and synthetics suggest that most of the waveform and deformation data were well explained (Fig. 5). The relative misfits of the teleseismic, strong-motion, high-rate GPS, and InSAR data are 0.43, 0.43, 0.62, and 0.09, respectively. A few teleseismic *P* waves, azimuths of which are around the fault strike (e.g., stations GUMO and DAV) were relatively poorly fitted. A major reason is that both the observed and synthetic *P* waves are weaker than those at other azimuths. The high-rate GPS data were not as well explained as the strong-motion data because of the relatively low signal-to-noise ratios. The InSAR deformation data were the best fitted because their Green's functions, which correspond to the earth responses at zero frequency, are not sensitive to the layering of the crustal structure.

Discussion

The fault model

The two-segment fault model was constructed from the sub-fault moment tensor solutions, which were determined based

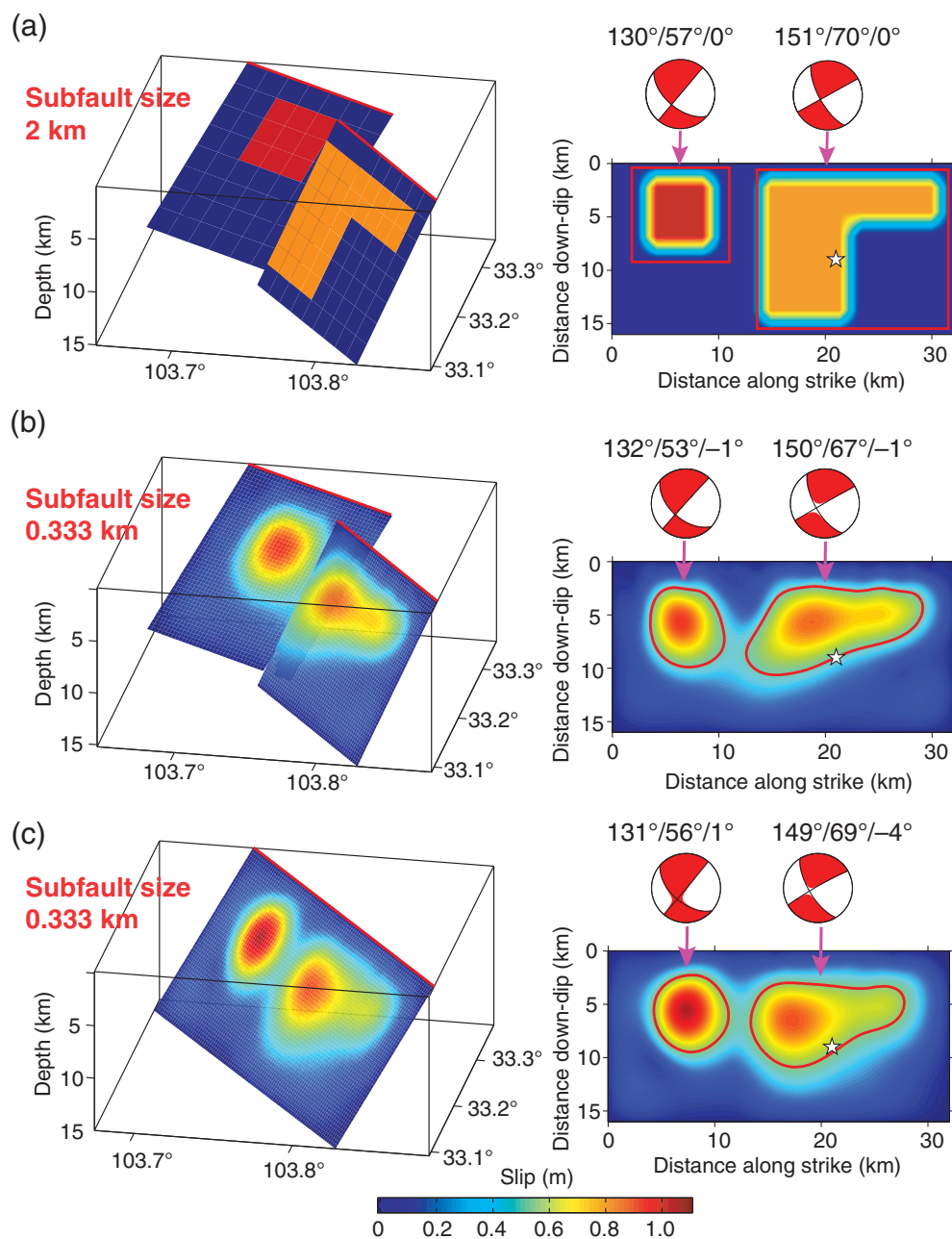


Figure 6. (a) Assumed two-segment fault model. (b) Model estimated from inversion on the two-segment fault. (c). Model estimated from inversion on a single-fault plane. On the left is the 3D view of the fault model and slip distribution and on the right is the slip distribution on the fault. The average mechanisms (focal mechanism plots) and fault parameters (strike/dip/rake) of each slip patch are labeled.

on a single fault. To check whether the results are dependent on the assumed fault model, we performed another inversion on the two-segment fault. The resulted misfit was 0.0434, slightly smaller than that of the single-fault inversion (0.0453) (Figs. S2, S6, and S7). The two-segment model (Fig. S6) was almost identical to the previous single-fault model (Fig. 3). The variations of strike, dip, and rake angles remain almost unchanged, suggesting that the subfault geometric parameters

are independent of the choice of the fault model. A significant difference is that the CLVD content was significantly reduced. This may be because the most significant change in fault geometry has been already incorporated in the two-segment inversion. It may imply that the changes in the fault geometry may account for the significant CLVD components near the slip gap (Fig. 3e).

The effectiveness of the geodetic inversion for complexity in fault geometry is also validated through a synthetic test. As shown in Figure 6, a slip model, which consists of two separated slip patches, is assumed on a two-segment fault. Accordingly, the two slip patches correspond to different geometries (Fig. 6a). The surface deformations are synthesized and added with Gaussian noise variance of 1 cm. By inverting the synthetic deformation data, the subfault moment tensors were estimated based on both two-segment and single-fault models (Fig. 6b,c). The misfit of the inversion on the two-segment fault model (0.0814) is slightly smaller than that on the single-fault model (0.0845). Not only the slip distributions but also the average mechanisms are well recovered in the two models (Fig. 6), confirming that the resultant focal mechanism derived from the geodetic inversion does not strongly

depend on the fault geometry assumed.

Our constructed two-segment fault model coincides well with the locations and mechanisms of the aftershocks. The fault traces of the two segments are consistent with the distribution of early aftershocks within 5 hr after the mainshock (Fig. 7 and Fig. S3; Zhang, Feng, *et al.*, 2017). In addition, aftershocks in the northwest are scattered along the southwest–northeast direction (Fang *et al.*, 2018), well

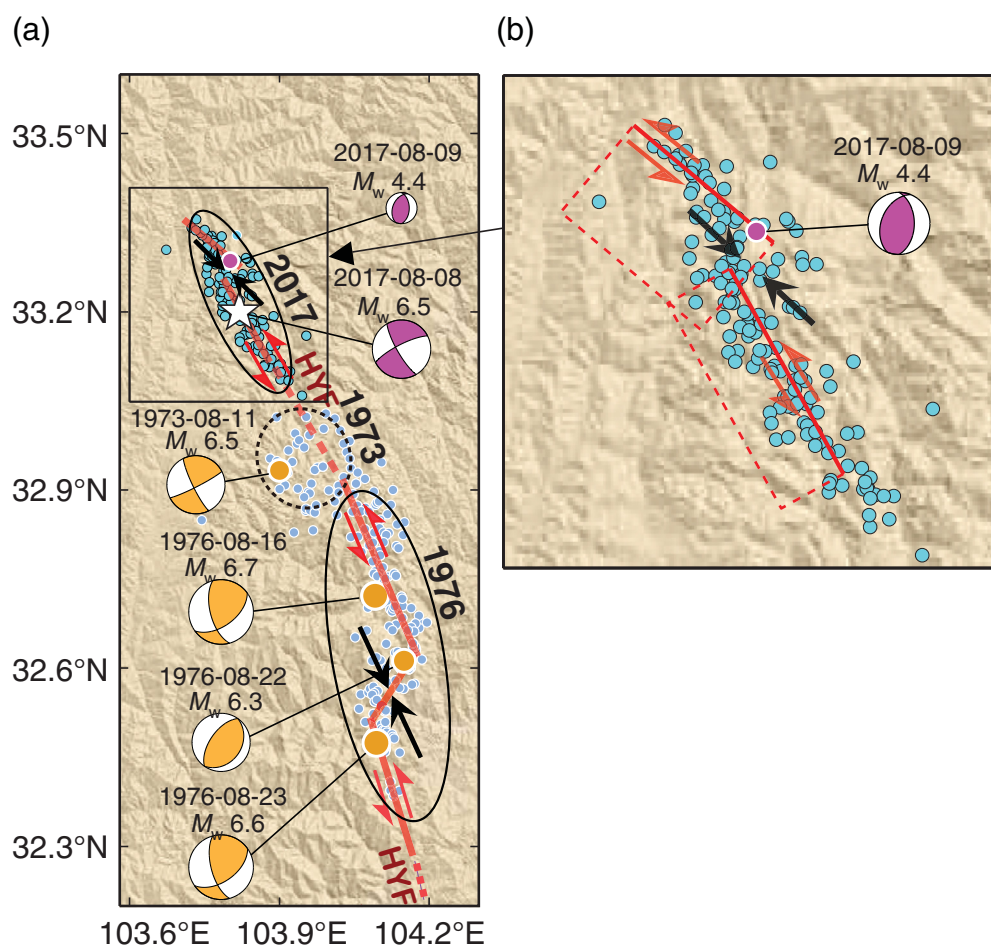


Figure 7. (a) Traces (bold red lines) of the HYF concluded based on the mechanism solutions of the 1976 Songpan earthquake sequences, the fault model of the 2017 Jiuzhaigou earthquake determined in this work, and their aftershock locations (Jones *et al.*, 1984; Zhang, Feng, *et al.*, 2017). Panel (b) panel amplifies the epicentral area of the 2017 Jiuzhaigou earthquake.

corresponding to the relatively gentle dip of the northwest segment. Particularly, the right-stepping of the two left-lateral strike-slip segments indicates a compressional stepover. This can be M_w supported by the aftershock mechanism results of Yi *et al.* (2017), who found an M_w 4.4 thrust aftershock around the stepover (Fig. 7), whereas other aftershocks are all strike-slip events.

The rupture model and its implications

Previous slip models of the 2017 Jiuzhaigou earthquake show variable features, which are strongly dependent on the data and variable methods used in their inversions. Most of the teleseismic waveform inversion studies found a single slip patch concentrated around the hypocenter, suggesting a disk-shaped rupture model (e.g., Zhang, Feng, *et al.*, 2017; Zhang *et al.*, 2021; Zheng *et al.*, 2017, 2020). In our teleseismic slip model, the slip expands to a larger area as a result of an assumed initiation area instead of an initiation point.

Previous strong-motion data inversion (Zheng *et al.*, 2017) suggested two slip patches, which were around the hypocenter and to the northwest of the epicenter. This is basically consistent with the strong-motion model obtained in this study (Fig. 3a). The InSAR deformations measured in other studies and in this work both confirm that the deformation area is broader in the northwest than the southeast (Ji *et al.*, 2017; Shan *et al.*, 2017). Through the geodetic inversion for the subfault moment tensors, we find that the northwest and southeast deformations are caused by gently dipping and steep segments, respectively. By jointly inverting the teleseismic, local waveform, and InSAR data, we build up a more complete model of the fault segmentation and rupture process of the earthquake.

The effectiveness of the joint inversion was verified by performing a resolution test (Fig. S8). Two isolated slip patches with different depth extensions were

assumed in the input model. The slip model estimated from the inversion of teleseismic and local waveform data recovers the major slip features at all depths. In contrast, the InSAR model constrains the slip at shallower depth better but has poor resolution at deeper depths. The joint inversion combines the advantages of the waveform inversion and the coseismic geodetic inversion, providing better constraints on the fault slips.

We calculated the stress drop based on the 2D Fourier transform of the coseismic fault slips (Andrews, 1980; Ripperger and Mai, 2004). The peak stress drops on the northwest and southeast segments are ~ 12 and 7 MPa, respectively. The difference in the stress drops may be associated with the geometric irregularities or roughness of the fault (Candela *et al.*, 2011). From Figure 3f, the strike of the northwest segment changes from $\sim 110^\circ$ to $\sim 150^\circ$. These significant changes in strike may lead to stress concentrations at the rupture front when it encounters geometric irregularities and hence larger

amounts of stress release once the rupture propagates through (Saucier *et al.*, 1992). In contrast, the strike of the southeast segment changes very little ($<10^\circ$), suggesting a nearly planar fault, on which stress accumulation would be lower and hence a smaller stress drop.

Comparison with the 1976 Songpan earthquake sequence

The fault segmentation of the 2017 Jiuzhaigou mainshock indicates that it ruptured two right-stepping and left-lateral strike-slip segments. Meanwhile, a compressional stepover between the two segments remained unruptured. This can be compared with the 1976 Songpan earthquake sequence (Jones *et al.*, 1984) to the south of the 2017 Jiuzhaigou event. Three major earthquakes ($M_w > 6$) of the 1976 Songpan earthquakes successively ruptured the HYF from north to south. Among them, the 22 August 1976 quake was a thrust faulting M_w 6.3 shock located between the two $M_w > 6.5$ oblique-slip shocks (Jones *et al.*, 1984; Fig. 7). The major difference between the 2017 Jiuzhaigou earthquake and the 1976 Songpan earthquake sequence is whether the rupture transformed through the stepover during a major earthquake. Our joint inversion slip model suggests two isolated slip patches on the southeast and north-west segments, implying that the ruptures of the 2017 shock may have gone through the stepover between the two strike-slip segments. However, in the 1976 Songpan earthquake sequence, the 16 August 1976 M_w 6.7 earthquake ruptures failed to jump from its own segment onto that ruptured by the 23 August 1976 M_w 6.6 earthquake. An important factor accounting for this difference may be the stepover width. Based on the fault segmentation model of the 2017 Jiuzhaigou earthquake, the stepover width was ~ 4 km (Fig. 7), which is close to the upper stepover limit for coseismic breaking following strike-slip ruptures found in general field investigations and dynamic simulations (Lettis *et al.*, 2002; Wesnousky, 2006). In the case of the 1976 Songpan earthquake sequence, the gap between the two strike-slip segments estimated from the relocated aftershocks was ~ 15 km (Jones *et al.*, 1984; Fig. 1c), which is at the upper limit of the maximum stepover width of 10–15 km ever observed, for example, from the 2001 M_w 7.8 Kunlun earthquake (Xu *et al.*, 2002; Antolik *et al.*, 2004) and the 2016 M_w 7.8 Kaikōura earthquake (Cesca *et al.*, 2017; Hamling *et al.*, 2017). Moreover, the compressional type may be another factor causing the failure of the rupture transformation in the 1976 earthquakes because it has been found that compressional stepover is more difficult to be jumped over than dilational stepover (Oglesby, 2005; Li and Liu, 2020). The similarity in fault segmentation of the 2017 Jiuzhaigou earthquake and the 1976 Songpan earthquake sequences indicates that they both occurred on the HYF. However, because of the different width of stepover between the strike-slip segments, the 1976 and 2017 earthquakes suggested quite different seismogenic patterns.

From dynamic modeling studies, compressional stepovers are hard to break in the mainshock but tend to generate strong aftershocks (Segall and Pollard, 1980). In the 1976 Songpan earthquakes, the 22 August M_w 6.3 shock ruptured the compressional stepover six days after the 16 August M_w 6.7 earthquake. Accordingly, for the 2017 Jiuzhaigou earthquake, strong aftershocks would be expected around the stepover. Up to date, only a thrust aftershock with $M_w > 4$ has been recorded there (Yi *et al.*, 2017), which may be insufficient to release the stress accumulated around the 4-km-sized slip gap (Fig. 7) if the fault is completely locked there. Therefore, future attention should be paid to the slip gap area to further investigate the possibility of strong aftershocks and slow fault slips.

Conclusions

Despite the moderate magnitude (M_w 6.5) of the 2017 Jiuzhaigou earthquake, the mainshock demonstrates a complex fault geometry and segmented rupture process. Coseismic slip reaches up to 1.0 m on the two right-stepping segments but are nearly negligible on the compressional stepover, which is consistent with results from previous dynamic modeling studies that compressional stepovers pose unfavorable conditions for rupture propagation but tend to generate strong aftershocks. The fault segmentation is similar to the 1976 Songpan earthquake sequence, but the rupture transformation is different: Ruptures of the 1976 earthquake sequence failed to jump over the stepover during the early strong mainshocks. Similar fault segmentations indicate that both the 1976 Songpan and the 2017 Jiuzhaigou earthquakes have likely ruptured along the HYF. However, because of the difference in stepover widths, the coseismic rupture patterns are distinctly different.

Data and Resources

The Sentinel Synthetic Aperture Radar (SAR) data were distributed free of charge by the European Space Agency (ESA). The teleseismic data were downloaded from the Incorporated Research Institutions for Seismology (IRIS) data center (http://ds.iris.edu/wilber3/find_event, last accessed August 2017). The strong-motion data were provided by the China Strong Motion Network Centre at Institute of Engineering Mechanics, China Earthquake Administration. The Global Positioning System (GPS) data were from the Crustal Movement Observation Network of China (CMONOC). The authors are grateful to aforementioned institutes for freely providing the data. The supplemental material contains a Word file that has eight figures and two tables and a txt file that gives the rupture model of the 2017 Jiuzhaigou earthquake.

Declaration of Competing Interests

The authors acknowledge that there are no conflicts of interest recorded.

Acknowledgments

This work was supported by the National Natural Science Foundation of China (NSFC; 41822401, 42021003, and 42074058).

References

- Andrews, D. J. (1980). A stochastic fault model 1. Static case, *J. Geophys. Res.* **85**, 3867–3877.
- Antolik, M., R. E. Abercrombie, and G. Ekström (2004). The 14 November 2001 Kokoxili (Kunlunshan), Tibet, earthquake: Rupture transfer through a large extensional step-over, *Bull. Seismol. Soc. Am.* **94**, no. 4, 1173–1194.
- Bassin, C., G. Laske, and G. Masters (2000). The current limits of resolution for surface wave tomography in North America, *Eos Trans. AGU* **81**, F897.
- Bouchon, M., and H. Karabulut (2008). The aftershock signature of supershear earthquakes, *Science* **320**, no. 5881, 1323–1325.
- Candela, T., F. Renard, M. Bouchon, J. Schmittbuhl, and E. E. Brodsky (2011). Stress drop during earthquakes: effect of fault roughness scaling, *Bull. Seismol. Soc. Am.* **101**, no. 5, 2369–2387.
- Cesca, S., Y. Zhang, V. Mouslopoulou, R. Wang, J. Saul, M. Savage, S. Heimann, S.-K. Kufner, O. Oncken, T. Dahm, et al. (2017). Complex rupture process of the M_w 7.8, 2016, Kaikoura earthquake, New Zealand, and its aftershock sequence, *Earth Planet. Sci. Lett.* **478**, 110–120.
- Das, S. (2007). The need to study speed, *Science* **317**, no. 5840, 905–906.
- Das, S., and C. Henry (2003). Spatial relation between main earthquake slip and its aftershock distribution, *Rev. Geophys.* **41**, no. 3, 1–16, doi: [10.1029/2002RG000119](https://doi.org/10.1029/2002RG000119).
- Deng, Q., P. Zhang, Y. Ran, X. Yang, W. Min, and Q. Chu (2003). Basic characteristics of active tectonics of China, *Sci. China Ser. D-Earth Sci.* **46**, no. 4, 356–372.
- Diao, G., X. Wang, G. Gao, X. Nie, and X. Feng (2010). Tectonic block attribution of the Wenchuan and Yushu earthquakes distinguished by focal mechanism types, *Chin. J. Geophys.* **53**, no. 5, 849–854.
- Fang, L. H., J. P. Wu, J. R. Su, M. M. Wang, C. Jiang, L. P. Fan, W. L. Wang, C. Z. Wang, and X. L. Tan (2018). Relocation of mainshock and aftershock sequences of M_s 7.0 Sichuan Jiuzhaigou earthquake, *Chin. Sci. Bull.* **63**, doi: [10.1360/N972017-01184](https://doi.org/10.1360/N972017-01184).
- Feng, W., Y. Tian, Y. Zhang, S. Samsonov, R. Almeida, and P. Liu (2017). A slip gap of the 2016 M_w 6.6 Muji, Xinjiang, China, earthquake inferred from Sentinel-1 TOPS interferometry, *Seismol. Res. Lett.* **88**, 1054–1064, doi: [10.1785/0220170019](https://doi.org/10.1785/0220170019).
- Han, L., J. Cheng, Y. An, Y. Fang, C. Jiang, B. Chen, Z. Wu, J. Liu, X. Xu, R. Liu, et al. (2018). Preliminary report on the 8 August 2017 M_s 7.0 Jiuzhaigou, Sichuan, China, earthquake, *Seismol. Res. Lett.* **89**, no. 2A, 557–569, doi: [10.1785/0220170158](https://doi.org/10.1785/0220170158).
- Hamling, I. J., S. Hreinsdóttir, K. Clark, J. Elliott, C. Liang, E. Fielding, N. Litchfield, P. Villamor, L. Wallace, T. J. Wright, et al. (2017). Complex multifault rupture during the 2016 M_w 7.8 Kaikōura earthquake, New Zealand, *Science* **356**, no. 6334, eaam7194.
- Huang, Y., J. Wu, T. Zhang, and D. Zhang (2008). Relocation of the $M_{8.0}$ Wenchuan earthquake and its aftershock sequence, *Sci. China Ser. D-Earth Sci.* **51**, no. 12, 1703–1711.
- Lettis, W., J. Bachhuber, R. Witter, C. Brankman, C. Randolph, A. Barka, W. Page, and A. Kaya (2002). Influence of releasing step-overs on surface fault rupture and fault segmentation: Examples from the 17 August 1999 Izmit earthquake on the North Anatolian fault, Turkey, *Bull. Seismol. Soc. Am.* **92**, no. 1, 19–42.
- Li, G., and Y. Liu (2020). Earthquake rupture through a step-over fault system: An exploratory numerical study of the Leech River fault, southern Vancouver Island, *J. Geophys. Res.* **125**, e2020JB020059, doi: [10.1029/2020JB020059](https://doi.org/10.1029/2020JB020059).
- Ji, L., C. Liu, J. Xu, J. Liu, E. Long, and Z. Zhang (2017). InSAR observation and inversion of the seismogenic fault for the 2017 Jiuzhaigou M_s 7.0 earthquake in China, *Chin. J. Geophys.* **60**, no. 10, 4069–4082.
- Jones, L. M., W. Han, E. Hauksson, A. Jin, Y. Zhang, and Z. Luo (1984). Focal mechanisms and aftershock locations of the Songpan earthquakes of August 1976 in Sichuan, China, *J. Geophys. Res.* **89**, 7697–7707.
- Kennett, B. L. N., E. R. Engdahl, and R. Buland (1995). Constraints on seismic velocities in the Earth from traveltimes, *Geophys. J. Int.* **122**, 108–124.
- Li, X., M. Ge, B. Guo, J. Wickert, and H. Schuh (2013). Temporal point positioning approach for real-time GNSS seismology using a single receiver, *Geophys. Res. Lett.* **40**, no. 21, 5677–5682.
- Li, X., M. Ge, X. Zhang, Y. Zhang, B. Guo, R. Wang, J. Klotz, and J. Wicket (2013). Real-time high-rate co-seismic displacement from ambiguity-fixed precise point positioning: Application to earthquake early warning, *Geophys. Res. Lett.* **40**, no. 2, 295–300.
- Oglesby, D. D. (2005). The dynamics of strike-slip step-overs with linking dip-slip faults, *Bull. Seismol. Soc. Am.* **95**, no. 5, 1604–1622.
- Ren, J., X. Xu, R. S. Yeats, and S. Zhang (2013). Millennial slip rates of the Tazang fault, the eastern termination of Kunlun fault: Implications for strain partitioning in eastern Tibet, *Tectonophysics* **608**, 1180–1200.
- Ripperger, J., and P. M. Mai (2004). Fast computation of static stress changes on 2D faults from final slip distributions, *Geophys. Res. Lett.* **31**, no. 18, doi: [10.1029/2004GL020594](https://doi.org/10.1029/2004GL020594).
- Saucier, F., E. Humphreys, and R. Weldon (1992). Stress near geometrically complex strike-slip faults: Application to the San Andreas fault at Cajon Pass, southern California, *J. Geophys. Res.* **97**, no. B4, 5081–5094.
- Segall, P., and D. D. Pollard (1980). Mechanics of discontinuous faults, *J. Geophys. Res.* **85**, no. B8, 4337–4350.
- Shan, X., C. Qu, W. Gong, D. Zhao, Y. Zhang, G. Zhang, S. Song, Y. Liu, and G. Zhang (2017). Coseismic deformation field of the Jiuzhaigou M_s 7.0 earthquake from Sentinel-1A InSAR data and fault slip inversion, *Chin. J. Geophys.* **60**, no. 12, 4527–4536.
- Simons, M., Y. Fialko, and L. Rivera (2002). Coseismic deformation from the 1999 M_w 7.1 Hector Mine, California, earthquake as inferred from InSAR and GPS observations, *Bull. Seismol. Soc. Am.* **92**, 1390–1402, doi: [10.1785/0120000933](https://doi.org/10.1785/0120000933).
- Sun, J., H. Yue, Z. Shen, L. Fang, Y. Zhan, and X. Sun (2018). The 2017 Jiuzhaigou earthquake: A complicated event occurred in a young fault system, *Geophys. Res. Lett.* **45**, no. 5, 2230–2240, doi: [10.1002/2017GL076421](https://doi.org/10.1002/2017GL076421).
- Wang, R., S. Heimann, Y. Zhang, H. Wang, and T. Torsten (2017). Complete synthetic seismograms based on a spherical self-gravitating Earth model with an atmosphere-ocean-mantle-core structure, *Geophys. J. Int.* **210**, no. 3, 1739–1764.
- Weng, H., and H. Yang (2017). Seismogenic width controls aspect ratios of earthquake ruptures, *Geophys. Res. Lett.* **44**, no. 6, 2725–2732, doi: [10.1002/2016GL072168](https://doi.org/10.1002/2016GL072168).
- Weng, H., J. Huang, and H. Yang (2015). Barrier-induced supershear ruptures on a slip weakening fault, *Geophys. Res. Lett.* **42**, no. 12, 4824–4832, doi: [10.1002/2015GL064281](https://doi.org/10.1002/2015GL064281).

- Wesnousky, S. G. (2006). Predicting the endpoints of earthquake ruptures, *Nature* **444**, no. 7117, 358.
- Xie, Z., Y. Zheng, H. Yao, L. Fang, Y. Zhang, C. Liu, M. Wang, B. Shan, H. Zhang, J. Ren, *et al.* (2018). Preliminary analysis about source characteristics and seismogenic structure of the Jiuzhaigou M_s 7.0 earthquake in 2017, *Sci. China Earth. Sci.* **61**, 339–352, doi: [10.1007/s11430-017-9161-y](https://doi.org/10.1007/s11430-017-9161-y).
- Xu, X., W. Chen, W. Ma, G. Yu, and G. Chen (2002). Surface rupture of the Kunlunshan earthquake (M_s 8.1), northern Tibetan plateau, China, *Seismol. Res. Lett.* **73**, no. 6, 884–892.
- Xu, X., G. Chen, Q. Wang, L. Chen, Z. Ren, C. Xu, Z. Wei, R. Lu, X. Tan, S. Dong, and F. Shi (2017). Discussion on seismogenic structure of Jiuzhaigou earthquake and its implication for current strain state in the southeastern Qinghai–Tibet plateau, *Chin. J. Geophys.* **60**, no. 10, 4018–4026.
- Yi, G., F. Leng, J. Liang, H. Zhang, M. Zhao, Y. Ye, Z. Zhang, Y. Qi, S. Wang, Y. Gong, *et al.* (2017). Focal mechanism solutions and seismogenic structure of the 8 August 2017 M 7.0 Jiuzhaigou earthquake and its aftershocks, northern Sichuan, *Chin. J. Geophys.* **60**, no. 10, 4083–4097.
- Yikilmaz, M. B., D. L. Turcotte, E. M. Heien, L. H. Kellogg, and J. B. Rundle (2015). Critical jump distance for propagating earthquake ruptures across step-overs, *Pure Appl. Geophys.* **172**, no. 8, 2195–2201.
- Zhang, X., W. Feng, L. Xu, and C. Li (2017). The source-process inversion and the intensity estimation of the 2017 M_s 7.0 Jiuzhaigou earthquake, *Chin. J. Geophys.* **60**, no. 10, 4105–4116.
- Zhang, X., L. S. Xu, L. Yi, and W. Feng (2021). Confirmation and characterization of the rupture model of the 2017 M_s 7.0 Jiuzhaigou, China, earthquake, *Seismol. Res. Lett.* doi: [10.1785/0220200466](https://doi.org/10.1785/0220200466).
- Zhang, Y., and R. Wang (2015). Geodetic inversion for source mechanism variations with application to the 2008 M_w 7.9 Wenchuan earthquake, *Geophys. J. Int.* **200**, no. 3, 1627–1635.
- Zhang, Y., W. Feng, Y. Chen, L. Xu, Z. Li, and D. Forrest (2012). The 2009 L'Aquila M_w 6.3 earthquake: A new technique to locate the hypocentre in the joint inversion of earthquake rupture process, *Geophys. J. Int.* **191**, 1417–1426, doi: [10.1111/j.1365-246X.2012.05694.x](https://doi.org/10.1111/j.1365-246X.2012.05694.x).
- Zhang, Y., R. Wang, and Y. T. Chen (2015). Stability of rapid finite-fault inversion for the 2014 M_w 6.1 South Napa earthquake, *Geophys. Res. Lett.* **42**, 10,263–10,272, doi: [10.1002/2015GL066244](https://doi.org/10.1002/2015GL066244).
- Zhang, Y., R. Wang, T. R. Walter, W. Feng, Y. Chen, and Q. Huang (2017). Significant lateral dip changes may have limited the scale of the 2015 M_w 7.8 Gorkha earthquake, *Geophys. Res. Lett.* **44**, 8847–8856, doi: [10.1002/2017GL074095](https://doi.org/10.1002/2017GL074095).
- Zheng, A., X. Yu, W. Xu, X. Chen, and W. Zhang (2020). A hybrid source mechanism of the 2017 M_w 6.5 Jiuzhaigou earthquake revealed by the joint inversion of strong-motion, teleseismic and InSAR data, *Tectonophysics* **789**, 228,538.
- Zheng, X., Y. Zhang, and R. Wang (2017). Estimating the rupture process of the 8 August 2017 Jiuzhaigou earthquake by inverting strong-motion data with IDS method, *Chin. J. Geophys.* **60**, no. 11, 4421–4430.
- Zhu, H., and X. Wen (2009). Stress triggering process of the 1973 to 1976 Songpan, Sichuan, sequence of strong earthquake, *Chin. J. Geophys.* **52**, no. 4, 994–1003.

Manuscript received 28 March 2021

Published online 11 August 2021